

See discussions, stats, and author profiles for this publication at: <https://www.researchgate.net/publication/50373536>

Alignment of Dispersions of Plate-Like Colloidal Particles of Ni(OH)(2) Induced by Elongational Flow

ARTICLE in THE JOURNAL OF PHYSICAL CHEMISTRY B · MARCH 2011

Impact Factor: 3.3 · DOI: 10.1021/jp108805m · Source: PubMed

CITATIONS

5

READS

81

5 AUTHORS, INCLUDING:



[Junaid Qazi](#)

The University of Calgary

12 PUBLICATIONS 72 CITATIONS

[SEE PROFILE](#)



[Jeffrey Penfold](#)

University of Oxford

532 PUBLICATIONS 13,308 CITATIONS

[SEE PROFILE](#)



[Isabelle Grillo](#)

Institut Laue-Langevin

142 PUBLICATIONS 2,530 CITATIONS

[SEE PROFILE](#)

Alignment of Dispersions of Plate-Like Colloidal Particles of Ni(OH)₂ Induced by Elongational Flow

S. Junaid S. Qazi,^{*,†,II} Adrian R. Rennie,[†] Ian Tucker,[‡] Jeff Penfold,[§] and Isabelle Grillo[†]

[†]Division of Materials Physics, Department of Physics and Astronomy, Uppsala University, Box 516, SE-751 20 Uppsala, Sweden

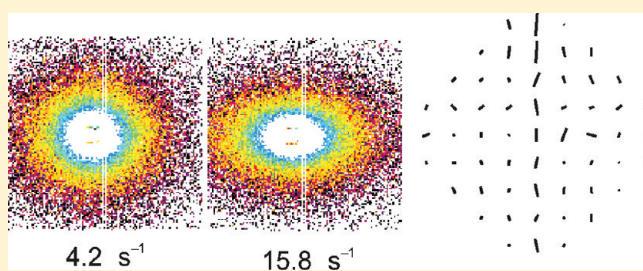
[‡]Unilever Research and Development, Port Sunlight Laboratory, Quarry Road East, Bebington, Wirral, U.K.

[§]ISIS Facility, STFC, Rutherford Appleton Laboratory, Chilton, Didcot, Oxon, U.K.

^IInstitut Laue Langevin, F-38042 Grenoble, France

 Supporting Information

ABSTRACT: Small-angle neutron scattering, SANS, has been used to study the alignment of a sterically stabilized colloidal dispersion of nickel hydroxide induced by elongational flow. Two different concentrations, 20 and 23 wt %, of well-defined hexagonal platelets have been studied. Significant anisotropy in the scattering patterns has been observed for the higher concentration dispersion that increases with increasing elongational strain rate. The effect of pipe flow (shear flow) on the orientational ordering at the inlets is also described. Near the outlets there is also a shear stress and this tends to increase the alignment. The orientational distribution of the particles under flow is described in terms of an order parameter calculated with respect to an individual director for each scattering pattern. The experimental measurements are supported by comparison with computer simulations which help to explain the effects of local velocity on the alignment induced by elongational flow. A slight decrease in the observed alignment was found after continuous flow for approximately 30 min and possible reasons are discussed.



Near the outlets there is also a shear stress and this tends to increase the alignment. The orientational distribution of the particles under flow is described in terms of an order parameter calculated with respect to an individual director for each scattering pattern. The experimental measurements are supported by comparison with computer simulations which help to explain the effects of local velocity on the alignment induced by elongational flow. A slight decrease in the observed alignment was found after continuous flow for approximately 30 min and possible reasons are discussed.

INTRODUCTION

Flow induced structural changes in concentrated colloidal dispersions are studied extensively in order to understand fundamental aspects of liquid behavior and rheology. They also have widespread and significant importance for practical applications. The changes in structure that occur in colloidal systems under shear flow have been reviewed recently.¹ A majority of studies have involved spherical particles, and significant differences are seen for dispersions with short and long-range interactions. Ashdown et al. described shear induced structural changes in charge stabilized polystyrene latex, where changes from a distorted crystal to sliding layers² were observed. Sterically stabilized poly(methyl methacrylate) latex formed aligned strings under shear³ and this resembled the structures predicted in the Brownian dynamics simulations of Heyes and Melrose.⁴ Dilute charge stabilized latex dispersions order in either body centered cubic or face centered cubic crystalline phase at rest which undergoes transition to flowing crystal structure at low shear rate, further increase in shear exhibits a transition from three to two-dimensional order in the dispersions⁵ and then one dimensionally ordered system of strings.⁶ The closed pack equilibrium structure undergoes a transition to sliding layers, flowing crystal and then amorphous order in the concentrated dispersion of latex particles.⁷ Recently more complex materials such as concentrated dispersions of the temperature sensitive poly(*N*-isopropylacrylamide) microgels have been studied and have been shown to form two-dimensional hexagonal close packed ordered

structures at high shear rate.⁸ Spherical particles that were dispersed in concentrated micellar solutions and exposed to simple shear displayed string-like structures at low shear rate and formed two-dimensional planar crystals at higher shear rates.⁹

Anisotropically shaped colloidal particles are of major practical relevance and importance where the orientation of the particles in a fluid will substantially affect the physical and optical properties of finished product. Colloidal dispersions and pastes are used as fillers in the paper industry, paints, and are also of great importance in the ceramic industry. Rheological properties are a crucial aspect in all these applications. Novel anisotropic food structures¹⁰ have been reported in protein-rich systems prepared by using well-defined flow geometries and patterns. Flow processing¹¹ is particularly important in the formation of colloidal microstructure in food products, where the control of alignment and order in all these dispersions largely determine their properties. The growth of helical bands¹² along the vorticity axis has been reported in dispersions of carbon nanotubes under shear flow.

Orientational ordering has been observed in dispersions of plate-like anisotropic particles under pipe flow^{13,14} and shear flow.¹⁵ However, there are few studies that have focused on elongational flow, and in many of these systems being able to

Received: September 15, 2010

Revised: January 31, 2011

Published: March 11, 2011

study the impact of elongational flow would provide an important new dimension to understanding flow induced phenomena. Ordering of multiwalled carbon nanotubes in extensional flow has been reported recently¹⁶ and this has led to better mechanical properties and higher melt strength. Increases in the elastic modulus and tensile strength in polyethylene/clay nanocomposites¹⁷ have also been reported under elongational flow. Extensional flow has also been applied to study the morphology of ethylene-vinyl acetate based layered silicate nanocomposites.¹⁸ The molecular configuration of single polymer molecules under elongational flow has been described,¹⁹ and they have been shown to form dumbbell, kinked and folded structures.

Some neutron scattering studies on the elongational flow induced alignment in mixed surfactants mesophases have been reported in previous work,^{20,21} using a specially designed crossed-slot elongational flow cell.²⁰ In those studies strong alignment under elongational flow was observed for the mixed surfactant lamellar fragments and rod-like micelles, even at relatively low flow rates.

In the measurements reported here, we have studied a model monodisperse colloidal dispersion of nickel hydroxide platelets. Small-angle neutron scattering has been used to study the flow-induced alignment of the dispersions under elongational flow; where the ability of neutrons to pass through thick samples allows us to study the interior or bulk of samples under conditions of elongational flow. The alignment of these colloidal dispersions has been studied previously under shear flow.²² At high concentrations a columnar structure is found with long stacks of particles that are arranged hexagonally.²³ For example, a weight fraction of 0.625 separates in to 70% columnar phase and 30% of another disordered phase.²² Shear thinning of these concentrated dispersions was observed and this was identified as corresponding to a transition from a columnar phase at low shear rates to sliding layers of uncorrelated particles at higher shear rates. The particles were seen to align with columns in the flow directions at low shear rates. Nickel hydroxide samples at lower concentrations between 0.579 and 0.606 weight fraction did not show alignment even under high shear rate up to $\sim 6000 \text{ s}^{-1}$ in a Couette cell.²² The elongational flow measurements describe here are for sample concentrations well below those at which such columnar phases are found and are in the range of isotropic and nematic liquids.

■ EXPERIMENTAL METHODS AND ANALYSIS

Sample Preparation. Uniform hexagonal platelets of nickel(II) hydroxide were prepared and sterically stabilized by adsorbing a sodium polyacrylate layer on the surface following the procedure reported by Brown et al.²³ They developed the original synthesis of Durand-Keklikian et al.²⁴ which uses controlled precipitation from dilute aqueous solution of nickel(II) nitrate and ammonium hydroxide. The average thickness of a single platelet was $\sim 6 \text{ nm}$ and the diameter was $\sim 105 \text{ nm}$. The thickness of the adsorbed stabilizing polymer layer was estimated to be 8.5 nm. The detailed method of characterization of the colloid is described in a previous paper.²⁵ For the synthesis, nickel(II) nitrate hexahydrate ($\geq 97.1\%$ pure) from Sigma-Aldrich, Prolabo ammonia solution 28% H₂O from VWR, and Dispex N40 from Ciba Chemicals were used, as supplied. The Dispex N40 acts as a charged steric stabilizer providing short-range repulsive forces that keep the particles stable even at high ionic strength in water. After preparation, the stabilized sample

was centrifuged and redispersed in D₂O (heavy water) and centrifuged again to the required experimental concentration. The estimated concentration of D₂O in the finally prepared sample was $\sim 97\%$. D₂O was used instead of H₂O as the solvent, as the reduced level of the incoherent scattering enables measurements with thicker sample path lengths. Samples with higher concentrations ($\sim 35 \text{ wt \%}$) were too viscous to obtain flow. The sample concentration was reduced to 23 wt % (~ 0.07 volume fraction) and then 20 wt % (~ 0.06 volume fraction) by the addition of D₂O. These concentrations are well below the overlap volume fraction, 0.18, for the nickel hydroxide particles calculated using the formula given by Jorgun and Zukoski.²⁶ This is the minimum concentration where the rotational motion of the anisotropic particles is restricted and is much less than the maximum packing fraction of such particles.

The dynamic viscosity as a function of shear strain rate for the dispersion of nickel hydroxide particles used in the neutron scattering experiments was measured several days after the experiment with an AR 2000 rheometer. Parallel plate geometry with a sample thickness of 0.25 mm was used and the sample was covered to avoid evaporation. For shear rates up to about 5000 s^{-1} the dynamic viscosity was seen to be approximately constant with a value of about 0.09 Pa s, that is, two orders of magnitude greater than that of water.

Measurement Details. An opposed jet flow cell with a recirculating pump, designed specifically for SANS measurements, was used.²¹ The original design criteria of the crossed-slot elongational flow cell,²⁷ used for small-angle X-ray scattering measurements, were modified for neutron scattering and the construction details of the cell have been described elsewhere.²¹ The cell has been used previously to study elongational flow induced ordering in surfactant mesophases.^{20,21} The central region of the cell has a fused quartz window with 24 mm outer diameter, and a viewable central region 20 mm in diameter. The input (along horizontal) and output (along vertical) flow channels are rectangular with a cross section of $\sim 10 \times 3.5 \text{ mm}$ and the length of each is $\sim 75 \text{ mm}$ which separate them well from the central region. Further modifications were made for these measurements in order to reduce the total required sample volume to about 50 mL.

The SANS measurements were made on the D22 diffractometer at the Institut Laue Langevin, Grenoble, France. A neutron wavelength of 8 Å was used with a collimation distance of 11.2 m. The sample to detector distance was 10 m. The distributions of scattered intensity, $I(Q)$ were measured on a 1 m \times 1 m 2-dimensional detector where the momentum transfer vector $Q = (4\pi/\lambda) \sin(\theta/2)$, λ is the wavelength and θ is the scattering angle. The measurable range of Q was between 0.004 \AA^{-1} and 0.056 \AA^{-1} . The detector captures scattering for Q directions that lie in the vertical plane and cover azimuthal angles between 0 and 2π . For all these measurements, except the sample at the concentration of 20 wt %, the sample path length was 3.5 mm. The sample was dispersed in D₂O and the transmission was measured to be 0.58. A B₄C/cadmium sandwich aperture with a diameter of 1 mm was used before the sample cell window so as to illuminate different small regions of the flow in XZ plane as shown in Figure 1. The scattering at different points of the flow field was determined by making a raster scan of the cell across the observation window and recording the separate scattering patterns with a counting time of 600 s per pattern. The flow rate through the cell was controlled by varying the voltage applied to the pump and was calibrated by measuring the volume of the

sample that came from the outlet during a given time with a measuring cylinder.

The schematic diagram of the elongational flow cell is shown in the Figure 1. The geometry of the elongational flow cell provides a nonuniform stress field in the circular window. The regions of the maximum compressional and elongational strain are along the horizontal and vertical directions. A more complex stress field exists at other places in the viewable window with smaller elongational strain rates and a small component of shear. The highlighted region in Figure 1, along the vertical axis, is the area with the maximum elongational strain. Data were collected at different positions over the entire central 20 mm diameter window of the cell which is shown by the dotted circle. The cell

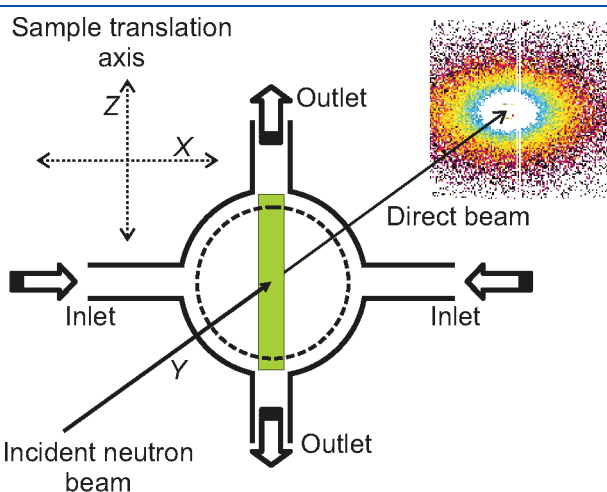


Figure 1. Schematic diagram of the experimental setup for the elongational flow experiment. The cell translates in the XZ plane to obtain the map of scattering over the viewable area of the cell. The highlighted area is the region of elongational strain where maximum alignment is observed at higher flow rate. The dotted circle represents the viewable window of the cell.

center is defined by the Cartesian coordinates and is at $(0, 0)$ and the centers of the different measured scattering patterns were separated by 2 mm in both the X and Z directions.

Measurements were made for three different flow rates 4, 12, and 15 mL s^{-1} , for the samples with a concentration of nickel hydroxide of 23 wt %. The SANS pattern obtained at the flow rate of 15 mL s^{-1} are shown in Figure 5. It is readily observed that the anisotropy in the scattering pattern along vertical axis increases with increasing flow rate. The scattering patterns at 4 mL s^{-1} and 12 mL s^{-1} for the same sample are shown in Figures S1, parts a and b, in the Supporting Information. Measurements were also made at a lower concentration of the nickel hydroxide dispersion, 20 wt %, and this showed no anisotropy in the scattering patterns, as illustrated in Figure S1c in the Supporting Information.

Simulation of Flow Pattern. A finite-element computation package²⁸ was used to make an approximate calculation of the flow pattern in the elongational flow cell. While full simulation of the nonlinear rheology in a complex geometry is difficult, recognition that the sample has a small range of local shear strain rate and so will be in a regime where the viscosity is approximately constant permits a simple calculation which will give some insight into the flow and enable further interpretation of the results. The simulation assumes a Newtonian fluid with a dynamic viscosity of the 0.09 Pa s as measured for the sample used in the neutron measurements and the density was taken to be 1.3 g cm^{-3} . Average flow velocities for the inlet and outlet regions were calculated from the overall flow rate. The velocities at the three different flow rates 4, 12, and 15 mL s^{-1} are 0.11, 0.35, and 0.43 m s^{-1} . As there are two inlets and outlets, the flow through each inlet and outlet is half of the total flow of the fluid. Flow patterns for an incompressible Newtonian fluid were calculated using these values and the resulting simulations at the minimum and maximum flow rates used here are shown in Figure 2.

The arrows in Figure 2 are along the local flow direction and the length corresponds to the local velocity of the sample. The dispersion enters through the inlets at different velocities for

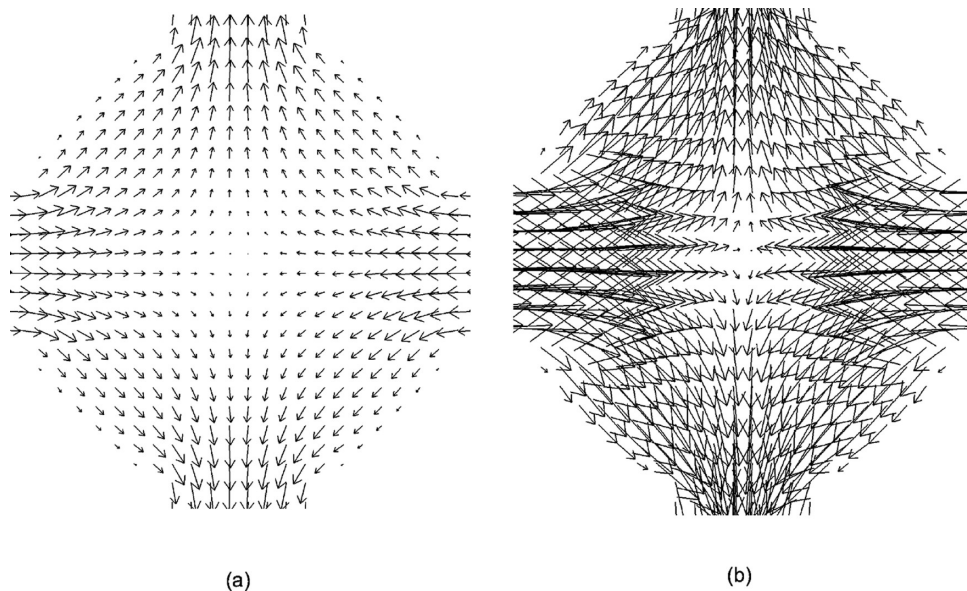


Figure 2. Simulations of the local velocity in the elongational flow cell for a Newtonian fluid at two different flow rates: (a) 4 mL s^{-1} ; (b) 15 mL s^{-1} . The plots show the decrease in velocity from inlet to the center and that it increases again toward the outlet. The length of each arrow is a measure of the value of the local velocity and the direction of arrows are along the local flow direction.

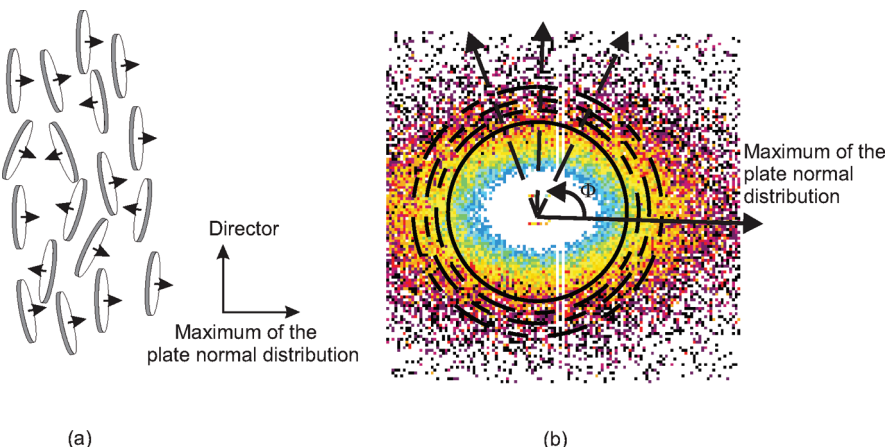


Figure 3. (a) Aligned platelets with their normal perpendicular to the director which is in the plane of the cell. (b) Horizontally elongated scattering pattern arises from the aligned plates in (a). Anisotropy in terms of an order parameter, S_2 , can be calculated by taking rings from the center to the boundary of each scattering pattern.

different overall flow rate which decreases from the inlet to the center and then increases again from the center of the cell toward the outlet. The velocity at the center is always $\sim 0 \text{ m s}^{-1}$ for each overall flow rate in the simulations. The data from the simulations enable the extensional strain rate, $d\nu/dz$, to be estimated, and is simply the derivative of the local velocity along the line from the center of the cell to the outlet. The simulations show that the extension rate increases in a region of less than 0.5 mm from the center of the cell and then remains approximately constant up to the outlet, for a given flow. The calculated values of the average extensional strain rate for the three flow rates used for the full raster maps, 4, 12, and 15 mL s^{-1} are 4.2, 12.8, and 15.8 s^{-1} , respectively. Plots of the local velocity for these flow rates along the extensional and compressional axes are given in Figures S3 and Figure S4 in the Supporting Information. The values of the local velocity are averaged over regions of 1 mm perpendicular to the flow because of the uncertainties in the numerical simulations. The values of average extensional and compressional strain rate from the numerical differentials of the local velocities in Figure S3 and S4 in the Supporting Information are shown against the flow rate in Figure S5 in the Supporting Information. These average values for the elongational and compressional strain rates can be compared with the experimentally observed orientational alignment as described below.

EVALUATION OF SCATTERING DATA

Alignment of the colloidal platelets gives rise to anisotropy in the scattering pattern and the extent of alignment in the preferred direction was determined quantitatively as described below. If the platelets are randomly oriented then the scattering patterns are isotropic. The distribution of intensity at a given scattering angle with respect to the azimuthal angle Φ can be described in terms of even Legendre polynomials^{14,29} which is analogous to the description of a periodic function as a Fourier series. Theoretical models of the alignment of anisotropic particles usually describe the extent of orientation in terms of order parameters defined by Legendre polynomials, $P_n(\cos \Phi)$, where the first even polynomial is³⁰ $P_2 = (3 \cos^2 \Phi - 1)/2$. An average order parameter, S_2 is calculated by considering the angle, Φ that the unique axis of each particle, e.g., the axis of a cylinder, makes with the vector known as the director that

lies in the direction of orientation provided by an external field. The order parameter, S_2 , for a distribution of many particles would then be

$$S_2 = \sum_i \langle (3 \cos^2 \Phi_i - 1)/2 \rangle / N \quad (1)$$

where the index i runs over all the N particles in the sample.

An analogous order parameter S_2 can be calculated from the distribution of scattered intensity, I as:

$$S_2(Q) = \frac{\int_{\Phi=0}^{2\pi} \left\langle I(\Phi i Q) \times \frac{1}{2}(3 \cos^2(\Phi) - 1) \right\rangle d\Phi}{\int_{\Phi=0}^{2\pi} \langle I(\Phi, Q) \rangle d\Phi} \quad (2)$$

where Φ is the azimuthal angle between Q and the director and integration is used to provide an appropriate average over all Φ from 0 to 2π . The calculated value is further normalized with the average intensity around the ring of scattering at a given amplitude of the vector Q . The scattered intensity, I , arises from all the particles in the sample and so no further explicit summation over the different particles is required. It is interesting to note that the evaluation of an order parameter defined by eq 2 has distinct differences to those calculated from other observations that might be obtained from eq 1. The small-angle scattering from a perfectly aligned distribution of particles does not lie on a single line and so the average S_2 will not be 1. The value will depend on the anisotropy of the scattering from a single particle. In contrast, a measurement of diffraction for a specific crystal plane from the internal structure of a perfectly aligned sample would occur in a single direction and so the theoretical maximum for S_2 would be unity.

The order parameters are calculated with respect to a single director and this choice has important consequences for the interpretation of the data. In the case of oriented long cylinders, it is common that the normal to the flat face (which is also the cylinder axis) and flow are both in the same direction which makes it very convenient to select the director in the plane of the cell and along the line of the maximum of the distribution of the axis of the cylinders and hence the flow direction. However for thin platelets such as the nickel hydroxide particles in the present study, it is expected that the flow induced alignment will be such that the normal to the flat face will be orthogonal to the flow

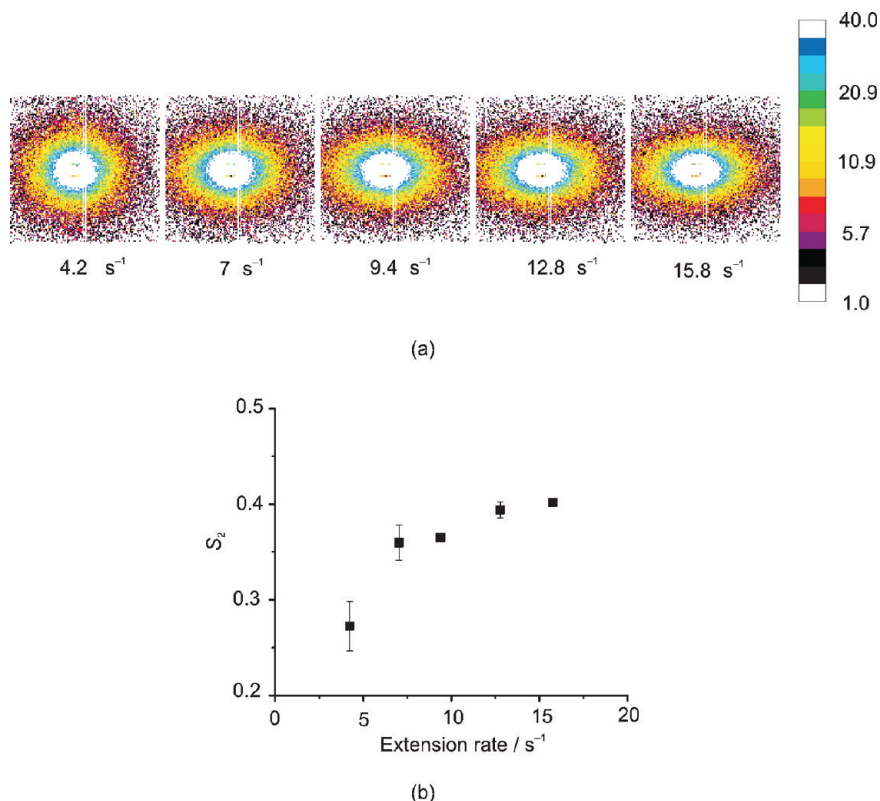


Figure 4. Alignment of the $\text{Ni}(\text{OH})_2$ platelets with increasing extension strain rate. (a) The scattering pattern at $(0, 0)$ for various extensional strain rates. (b) Values of S_2 calculated for the pattern in part a as a function of extensional strain rate. The anisotropy in the scattering patterns increases as the elongational strain rate increases. The data presented is for the sample at 23 wt % of $\text{Ni}(\text{OH})_2$.

direction. This requires a different selection of the director for the calculation of S_2 that corresponds to the different geometry of the particles and their orientation with respect to the flow. We have therefore selected the director to be in the plane of the cell and orthogonal to the maximum in the orientation distribution of the normal of the flat faces of the disks. If the plates are aligned vertically, as shown in Figure 3a, they will give rise to anisotropy in the scattering patterns that are elongated in the horizontal direction as shown in Figure 3b. The order parameters, S_2 , for individual scattering patterns in Figure 4a, Figure 5 and Figure S1 in the Supporting Information are then calculated using eq 2 but with the cosine replaced by a sine function. This is equivalent, at the center of the cell, to taking the director as vertical and this is chosen so that the order parameter becomes larger as the orientational alignment increases. For other positions in the cell, the origin of Φ is rotated to lie on the line of anisotropy of the scattering pattern. The calculations are made for an annulus in each scattering pattern from $Q = 0.0102$ to 0.0337 \AA^{-1} with step of 0.00078 \AA^{-1} . The Q range is selected to include the largest possible area of the detector while avoiding the edges and the region around the beam stop in the calculations. In the present study, S_2 does not vary significantly with Q (as shown in the Supporting Information in Figure S2). Hence an average is taken over a large range of Q values. However in other experiments it can be useful to analyze the changes in orientation at different length scales by considering S_2 as a function of Q . If the scattering patterns are fully isotropic then $S_2 = 0.25$. The scattering from cylindrical object has been described by Pedersen³¹ and it is possible to estimate the maximum value of S_2 that would be observed in this range of Q for particles with the shape that has

been used for this study as about 0.55. If the value is greater than 0.25 then the particles are aligned with the maximum in the distribution of the disk normals perpendicular to the flow direction. If the value is less than 0.25 then the alignment, on average, will be rotated by 90° to the reference direction.

RESULTS AND DISCUSSION

For clarity, the results are presented in four parts. First the behavior of nickel hydroxide platelets at the stagnation point with increasing flow rate is discussed. Second, the variation in induced order across the window of the elongational flow cell is presented and discussed. Next the trends of change along the compressional and elongational axes and the effects of the inlets and outlets on particle alignment are discussed and finally the elongational and shear strains are compared in terms of dimensionless numbers.

(a). Flow Rate Dependence at Stagnation Point. The opposing jet flow cell gives rise to flow pattern and stress on the sample that is not uniform. The simulations of this pattern are represented by the maps of velocity shown in Figure 2, parts a and b. The cell is planar and was maintained perpendicular to the incident beam and so no direct information from scattering is obtained in the direction of the shear gradient that is present at most places across the thickness of the cell (Y -direction). At the geometric center of the cell, there is a stagnation point with zero velocity. As the fluid velocity is zero across the thickness of the cell, the only gradient in strain at this point is elongational (vertical, Z -direction) or compressional (horizontal, X -direction). At other points in the cell there are gradients in magnitude and

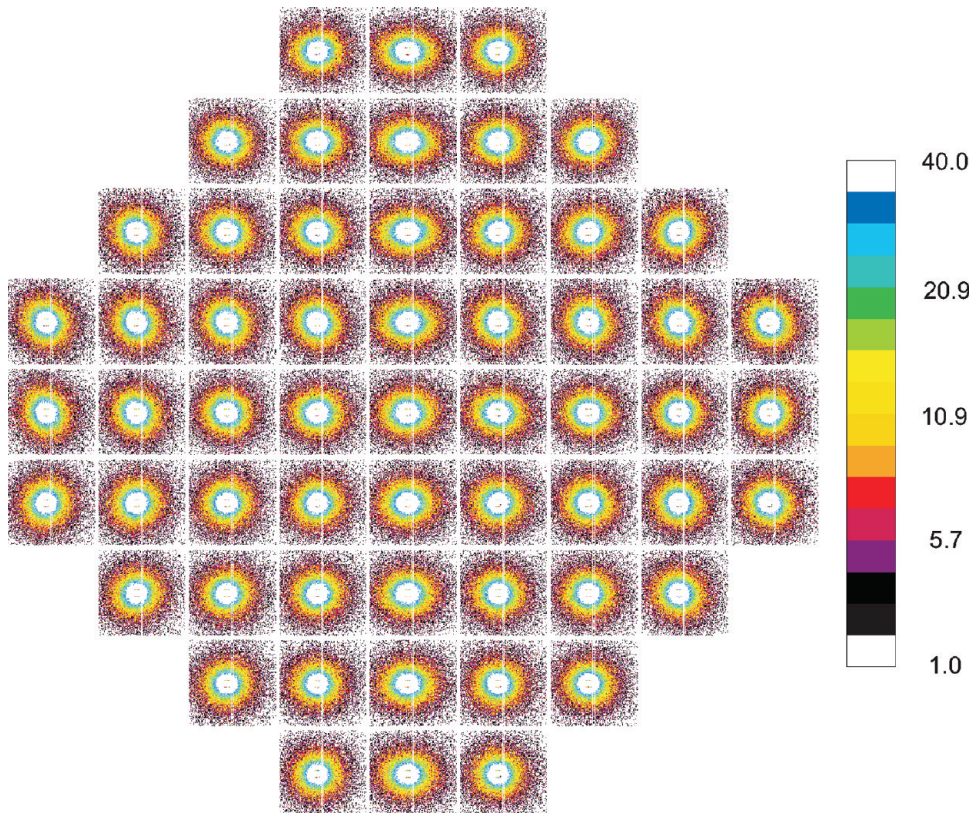


Figure 5. Scattering patterns for 23 wt % $\text{Ni}(\text{OH})_2$ at the flow rate of 15 mL s^{-1} , data sets are more anisotropic along the vertical axis where particles experience high elongational strain rate. Calculated values of S_2 for the map are shown in Figure 6a. The patterns are less anisotropic as we lower the flow rate. The scattering maps for 4 and 12 mL s^{-1} are presented in the Supporting Information.

direction of the velocity and hence the shear strain is not zero both in the XZ -plane and in the Y -direction as mentioned previously. These are discussed further below. SANS measurements were made for each sample at the center of the cell (coordinate position $(0, 0)$, the stagnation point) at different flow rates in order to establish the optimal flow rate for maximum alignment before measuring the full raster maps. The resulting scattering patterns are shown for 23 wt % $\text{Ni}(\text{OH})_2$ in D_2O in Figure 4a.

The scattering patterns in Figure 4a measured at the center of the cell show a significant increase in anisotropy as the extensional strain rate increases. Values of S_2 from the scattering patterns in Figure 4a are plotted against the average value of elongational strain rate in the Figure 4b. The data in Figure 4b shows that the alignment in the particles increases between the flow rates of 4 and 12 mL s^{-1} and tends to a plateau at the higher flow rates.

It is clear that the scattering patterns were more anisotropic at the start of the experiment in the initial measurements shown in Figure 4a as when compared with those measured later. The later measurements are shown in the raster maps of scattering at different points in the cell in Figure 5 and Figure S1 (in the Supporting Information). Dynamic light scattering measurements on diluted specimens of the sample after the neutron scattering and flow experiment did not show any significant change in the size distribution to that observed in the initial characterization. The sample was observed to be less viscous after the neutron measurements that involved continuous flow for about 1 day. However we could not measure the rheological

properties immediately after the experiments as a rheometer was not available. The dynamic light scattering results suggest that one can rule out damage to the particles as the cause of the change in the physical properties with time. A possible explanation for the changes might be an initial decrease in the local ordered structure or in loose aggregation of the particles that is disrupted by the flow. Similar effects have been observed in dispersions of lamellar fragments.³² An alternative explanation is that the change could arise from a reduction in air bubbles that arise during the initial stages of filling the cell. Working the solution under extreme flow conditions could cause the dispersion to become more effectively degassed and responsible for the change in apparent viscosity. However, the flow was uniform when the neutron measurements started.

(b). Comparison of the Spatial Variation of Order with the Flow Pattern. The full raster of scattering patterns for the circular window of the flow cell were measured when the sample viscosity had reached equilibrium. The data from these measurements are shown in Figure 5 for 23 wt % dispersion at a flow rate of 15 mL s^{-1} and Figure S1 (in the Supporting Information) for 23 wt % dispersion at 4 and 12 mL s^{-1} and for 20 wt % dispersion at a flow rate of 28 mL s^{-1} . The line through the center of the cell on the vertical (Z) axis is the region with the highest elongational strain rate. There is little anisotropy in the scattering patterns along the vertical axis for the sample at 23 wt % concentration for the flow rate of 4 mL s^{-1} . The anisotropy increases along the vertical axis as the flow rate increases. The particles experience more elongational strain along the vertical axis which induces alignment. The scattering patterns are more anisotropic at the flow rate of 12 mL s^{-1}

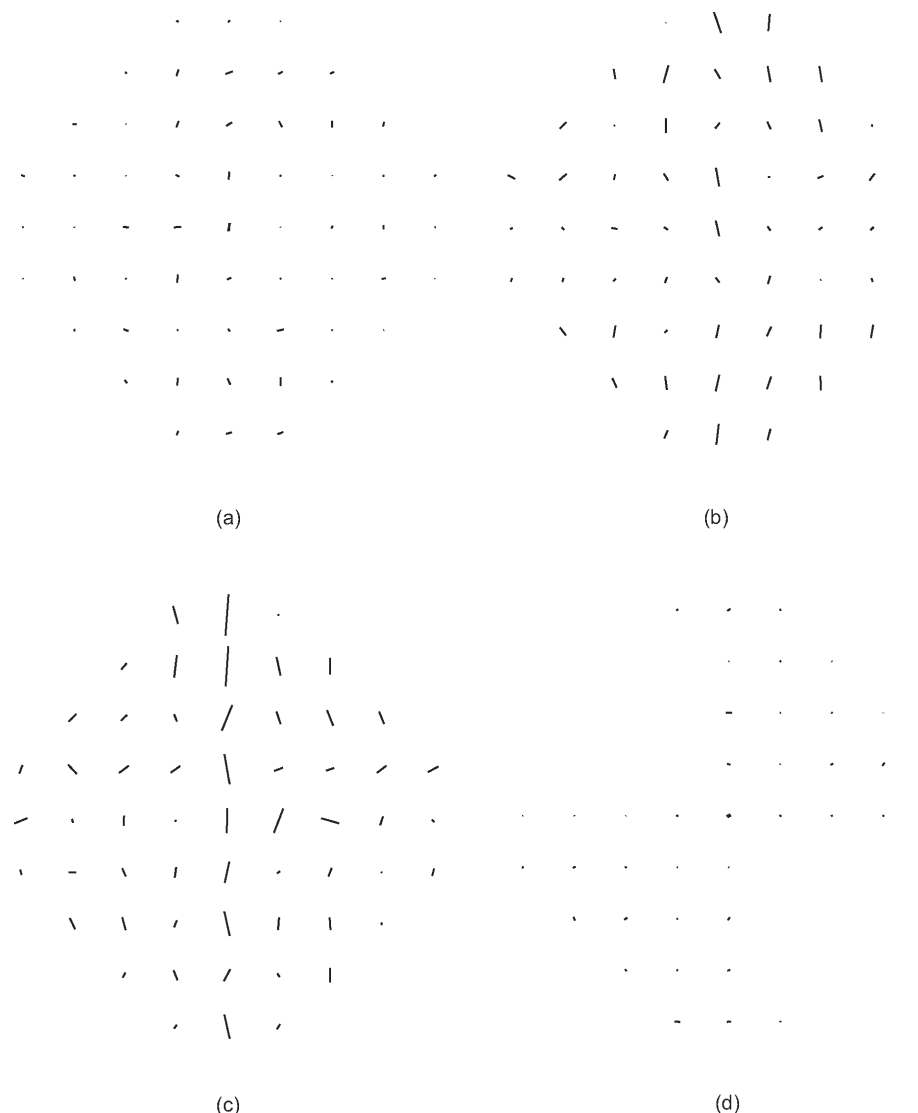


Figure 6. Calculated values of S_2 are plotted. The lines are along the director and the extent of alignment is represented by the length of each line in the map. (a), (b) and (c) are for the sample at 23 wt % nickel hydroxide dispersion at 4, 12 and 15 mL s^{-1} respectively. The maps show that the alignment increases as the flow rate increases. (d) A map from the sample at 20 wt % nickel hydroxide and with 6 mm path length does not show pronounced alignment. The maximum length of the line at the upper outlet of the cell in (c) corresponds to $S_2 \sim 0.35$ and the dots in the raster maps shows $S_2 \sim 0.25$. The scattering patterns corresponding to (b), (c) and (d) are shown in the Supporting Information.

which further increases at the flow rate of 15 mL s^{-1} as shown in Figure 5 and Figure S1 in the Supporting Information. Some measurements were made on a sample with 20 wt % nickel hydroxide and with a 6 mm path length, which gives much higher flow rate. The particles at this concentration showed no orientation even at a flow rate of 28 mL s^{-1} , as shown in the scattering patterns in Figure S1c in the Supporting Information.

The anisotropy in the scattering patterns, as quantified by S_2 , is plotted along the chosen director in Figure 6. The director is effectively defined so as to be in the local flow direction as discussed above. The maximum value of S_2 calculated from the scattering patterns is ~ 0.4 . The length of the line represents the calculated value of S_2 and its orientation is the director; and so describes the extent of alignment of the platelets at each position in the flow cell, as shown in Figure 6. The lines are much longer along the vertical axis in part c, which decreases in part b and further in part a as the flow rate decreases. The sample at 23 wt %

concentration shows significant increase in alignment as the elongational strain rate increases as shown from part a to part c. The order parameter map in Figure 6d is for the data from the sample with 20 wt % concentration. The completely random direction of the lines with their short amplitude confirms that there is no significant alignment of the particles at this concentration.

The patterns in parts a–d of Figure 6 show little or no orientational order. In parts b and c of Figure 6, the maximum alignment is in the direction of the maximum elongational strain rate (vertical Z axis). Along the horizontal axis the alignment is much less and does increase with flow rate, and reflects the pipe flow or shear gradient contribution in addition to the elongational component. The off-axis positions vary in degree or order of orientation, such that for Figure 6, parts b and c. The general pattern of observed anisotropy in scattering is consistent with the simulations shown in Figure 2.

The results show that there is no significant change in the alignment under the compressional strain from the inlet to the center of the cell. The points measured near but not at the center on the compressional axis for the flow at 15 mL s^{-1} do show some alignment. However the scattering pattern at $(2, 0)$ is less anisotropic than that measured at $(-2, 0)$. This is reflected in the values of S_2 shown in Figure 6c for these data sets. This observation suggests that the center of flow in the cell is slightly misaligned in the horizontal direction for this measurement, perhaps due to small difference in the pressure or flow at the two different inlets. Therefore, at the position $(2, 0)$ there is possibly significant elongational strain that causes alignment. It is unlikely that the observed orientation arises from compressional stress. The calculated values of S_2 at the center of the cell in Figure 6a is approximately equal to that of in Figure 4b while for the flow rates of 12 and 15 mL s^{-1} , in Figure 6, parts b and c, the values from the raster maps at the center of the cell are 0.29 and 0.31, respectively. These values of S_2 are less than those shown in Figure 4b that were determined from the short initial series of measurements. This difference was attributed to the change in viscosity that was observed during the experiment, as discussed earlier.

(c). Changes along the Compressional and Elongational Axes—the Role of Inlet and Outlet of the Cell. The variation in the order parameter S_2 along the horizontal (inlet to the center of the cell) and vertical direction (center of the cell to the outlet) is plotted against the local velocity in Figures 7 and 8 respectively. The local velocity decreases from the inlet to the center of the cell and then increases from the center of the cell to the outlet. The sample measured at the flow rates of 4 and 12 mL s^{-1} does not show alignment along the horizontal axis in Figure 7. The value of S_2 is not uniform along the horizontal axis at the flow rate of 15 mL s^{-1} : S_2 decreases from the inlet to about half way to the center and then increases. The slightly higher values of S_2 at the inlet at 15 mL s^{-1} could reflect the contribution from pipe flow that provides a shear gradient. At the inlet, the particles tend to align with their plate normals perpendicular to the horizontal axis (i.e., the plane of the disks lies in the flow direction). The alignment decreases and then increases abruptly at the center of the cell as the particles rotate by 90 deg under the elongational stress. These changes are reflected in the anisotropy of the scattering patterns shown in Figure 5.

Significant effects of the increase in strain rate are observed along the vertical line of maximum elongational stress. The strain rate is approximately constant for a given flow rate at each point on this line. Figure 8 shows that S_2 increases with the flow rate and reproduces the trend shown in Figure 4. However at the lowest flow rate, no significant orientation was observed. For the intermediate flow rate of 12 mL s^{-1} the alignment increases as the velocity increases on the line from the center to the outlet. For the highest flow rate that was measured, 15 mL s^{-1} , the alignment is approximately constant except at the outlet. The value of S_2 is slightly higher for 12 and 15 mL s^{-1} at the outlet. This outlet is to the pipe which feeds the sample back to the reservoir. Higher values of S_2 could reflect the contribution in the alignment from the shear gradient at the outlets. At the center of the cell the velocity is zero and so the orientation that is observed at this point is purely due to the elongational stress and not shear.

The changes in alignment that are seen for the intermediate flow rate suggest that the orientation does not just depend on the local value of the elongational strain rate that does not vary significantly for the points shown. The increase in alignment

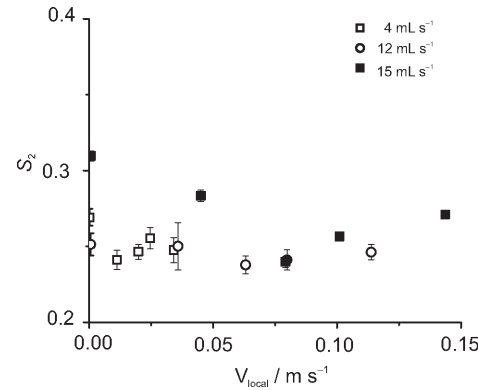


Figure 7. Calculated values of order parameters, S_2 , from the original scattering patterns are plotted against the local velocity of the sample along the horizontal axis of the cell calculated from the simulation for three different flow rates, 4 , 12 , and 15 mL s^{-1} . The plot shows that there is no effect of compression strain rate on the alignment in the particles at the measured flow rates.

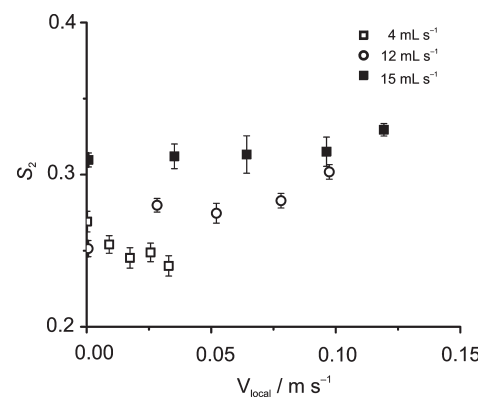


Figure 8. Values of order parameters S_2 calculated from the original scattering patterns are plotted against the local velocity of the sample obtained from the simulation for three different flow rates at points in the cell along the vertical axis. There is no alignment at the flow rate of 4 mL s^{-1} . A flow rate of 12 mL s^{-1} shows alignment of the particles that increases from the center of the cell to the outlet. At the flow rate of 15 mL s^{-1} , alignment is higher but remains almost constant in the region of elongational strain.

could be due to the time taken for reorientation under a given stress. The average time of transit for a particle through the cell in this flow is of the order of a second at the maximum flow rate. In Figure 8, the points for each flow rate could be considered as representing different times for which the particles have experienced an approximately constant elongational strain rate. This residence time is apparently not very important in determining the extent of orientation for the lowest and highest measured flow rates. For the intermediate flow rate there is a change of S_2 that depends on either the local velocity or the residence time. Even though the particles experience a longer residence time at the lowest flow rate, this is not sufficient to induce alignment at the extensional strain rate in the cell. At the highest flow the residence time is less but the maximum order is already reached very close to the center of the cell. The results show that an elongational strain rate $\sim 16 \text{ s}^{-1}$ effectively induces significant order in this dispersion. Alignment under shear flow at this strain rate was observed for a much higher concentration with a transition from a columnar to an uncorrelated layer structure.²²

(d). Comparisons of Elongational and Shear Strain Rates. At the stagnation point we have investigated elongational strain rates up to about 16 s^{-1} . The maximum fluid velocity is found at the inlets and outlets and this will give the maximum values of $\dot{\gamma}_Y$. These are about 70 s^{-1} at the maximum flow rate. The shear gradients in the XZ-plane are smaller and at the highest flow rate have magnitudes of less than 10 s^{-1} . It is interesting to observe that the strain rates both for elongation and for shear are much smaller than those required to align dilute samples of similar size and concentration in a previous study where the strain was purely shear.²² For the purposes of comparison with studies of other materials, it is sometimes helpful to consider scaling arguments or dimensionless numbers. Studies of shear flow often report the Peclet number that can be considered as the ratio of the energy associated with the shear strain to the thermal energy. This is usually defined as

$$P_e = 6\pi\eta_s a^3 \dot{\gamma} / k_B T$$

where η_s is the shear viscosity, $\dot{\gamma}$ is the shear strain rate, T is the absolute temperature, k_B is Boltzmann's constant, and a is a characteristic dimension such as the size or separation of particles in the fluid. If P_e is less than unity particles will be readily randomized by thermal motion but when P_e is greater than 1, they may be aligned or the structure in the fluid can be modified by the flow. Sometimes it is assumed that the viscosity of the pure solvent may be the appropriate variable to consider for dilute dispersions. We can use the values of the shear strain rates mentioned in the previous paragraph to estimate a Peclet number. It is also possible to consider a similar quantity for an extensional flow that we designate P_1 and is given by

$$P_1 = 6\pi\eta_1 a^3 \dot{\varepsilon} / k_B T$$

where η_1 is the elongational viscosity, $\dot{\varepsilon}$ is the elongational strain rate, and a is a characteristic dimension appropriate to the particles and the deformation. For many molecular liquids, the elongational viscosity is difficult to determine as they do not sustain significant elongational stress. Trouton's rule^{33,34} suggests that for uniaxial stain $\eta_1 = 3\eta_s$. In the absence of specific data for the sample measured and assuming that a is the diameter of the particles we obtain values of P_1 equal to 2.3 at the center of the cell and P_e equal to 3.4 for shear strain in the Y direction at the exit of the cell for the maximum flow rate reported. P_e is zero at the center of the cell. These values of Peclet number provide an approximate guide for intercomparison with other materials and flow patterns but clearly can not account fully for the effects of strain in a complex geometry. Care must also be taken as some authors choose to use different numerical prefactors in the definition of Peclet number.

CONCLUSIONS

The orientational order of a concentrated colloidal dispersion of nickel hydroxide has been studied under elongational flow. The properties of this well-defined colloidal dispersion of platelets can be rationalized as a model system of hard disks. The alignment of the particles increases as the elongational strain rate increases. Higher degrees of alignment are observed in the region of flow where there is strong elongational stress and also increases with flow rate. Computer simulations for a Newtonian fluid under similar flow conditions provide a means to compare the extent of alignment with the local velocity of the flowing sample: the simulations replicate reasonably well the observed

patterns of orientation. The results demonstrate that the alignment does not depend only on either the local velocity or the velocity gradients. The induced order arises primarily from elongational strain at the center of the cell where the local velocity is always zero for any flow rate. The compression along the horizontal direction does not induce any significant alignment; however the alignment increases as the elongational strain rate increases. The flow induced orientational order depends strongly upon dispersion concentration, and measurements at lower colloidal (<20 wt %) concentrations showed no alignment.

ASSOCIATED CONTENT

S Supporting Information. Scattering patterns at the flow rates of 4 and 12 mL s^{-1} for the 23 wt % sample at a flow rate of 28 mL s^{-1} for the 20 wt % sample (Figure S1, parts a–c, respectively), an example of the values of S_2 at different Q for a highly aligned sample (position (0, 0) in the flow cell for a flow rate of 15 mL s^{-1} (Figure S2), local velocity along the compressional and extensional axes for the flow rates used in the studies (Figure S3 and S4, respectively), and numerical differentials of the local velocities (Figure S5) for different flow rates which correspond to the extensional and compressional strain rates. This material is available free of charge via the Internet at <http://pubs.acs.org>.

AUTHOR INFORMATION

Corresponding Author

*Telephone: +46 18 471 3522. E-mail: Junaid.Qazi@fysik.uu.se.

Notes

¹On study leave from COMSATS Institute of Information Technology, Pakistan.

ACKNOWLEDGMENT

We are grateful to the ILL for an allocation of beam time for these measurements and to Peter Cross, David Bowyer and Steven Rowe for technical support in preparing the SANS measurements. This work has been supported in part by the Swedish Research Council (VR).

REFERENCES

- Vermant, J.; Solomon, M. *J. Phys: Condens. Matter* **2005**, 17, R187–R216.
- Ashdown, S.; Marković, I.; Ottewill, R. H.; Lindner, P.; Oberthür, R. C.; Rennie, A. R. *Langmuir* **1990**, 6, 303–307.
- Clarke, S. M.; Ottewill, R. H.; Rennie, A. R. *Adv. Colloid Interf. Sci.* **1995**, 60, 95–118.
- Heyes, D. M.; Melrose, J. R. *J. Non-Newtonian Fluid Mech.* **1993**, 46, 1–28.
- Ackerson, B. J.; Clark, N. A. *Phys. Rev. A* **1984**, 30, 906–918.
- Ackerson, B. J.; Clark, N. A. *Physica A* **1983**, 118, 221–249.
- Ackerson, B. J.; Hayter, J. B.; Clark, N. A.; Cotter, L. *J. Chem. Phys.* **1986**, 84, 2344–2349.
- Stieger, M.; Lindner, P.; Richtering, W. *J. Phys: Condens. Matter* **2004**, 16, S3861–S3872.
- Pasquino, R.; Snijkers, F.; Grizzuti, N.; Vermant, J. *Langmuir* **2010**, 26, 3016–3019.
- Manski, J. M.; Van der Goot, A. J.; Boom, R. M. *Trends Food Sci. Technol.* **2007**, 18, 546–557.
- Walkenström, P.; Hermansson, A. M. *Curr. Opin. Colloid Interface Sci.* **2002**, 7, 413–418.

- (12) Ma, A. W. K.; Mackley, M. R.; Rahatekar, S. S. *Rheol. Acta* **2007**, *46*, 979–987.
- (13) Rennie, A. R.; Bare, S.; Cockcroft, J. K.; Jupe, A.; *C. J. Colloid Interface Sci.* **2006**, *293*, 475–482.
- (14) Barè, S.; Rennie, A. R.; Cockcroft, J. K.; Colston, S. L.; Jupe, A. C. *J. Appl. Crystallogr.* **2001**, *34*, 573–579.
- (15) Ramsay, J. D. F.; Lindner, P. *J. Chem. Soc. Faraday Trans* **1993**, *89*, 4207–4214.
- (16) Dintcheva, N. T.; Arrigo, R.; Morreale, M.; Mantia, F. P. L.; Matassa, R.; Caponetti, E. *Polym. Adv. Technol.* **2010**, *10.1002/pat.1648*.
- (17) Mantia, F. P. L.; Dintcheva, N. T.; Scaffaro, R.; Marino, R. *Macromol. Mater. Eng.* **2008**, *293*, 83–91.
- (18) Prasad, R.; Pasanovic-Zujo, V.; Gupta, R. K.; Cser, F.; Bhattacharya, S. N. *Polym. Eng. Sci.* **2004**, *44*, 1220–1230.
- (19) Perkins, T. T.; Smith, D. E.; Chu, S. *Science* **1997**, *276*, 2016–2021.
- (20) Penfold, J.; Tucker, I. *J. Phys. Chem. B* **2007**, *111*, 9496–9503.
- (21) Penfold, J.; Staples, E.; Tucker, I.; Carroll, P.; Clayton, J.; Cowan, J. S.; Lawton, G.; Amin, S.; Ferrante, A.; Ruddock, H. *J. Phys. Chem. B* **2006**, *110*, 1073–1082.
- (22) Brown, A. B. D.; Rennie, A. R. *Phys. Rev. E* **2000**, *62*, 851–862.
- (23) Brown, A. B. D.; Clarke, S. M.; Rennie, A. R. *Langmuir* **1998**, *14*, 3129–3132; *Langmuir* **1999**, *15*, 1594.
- (24) Durand-Keklikian, L.; Haq, I.; Matijevic, E. *Colloids Surf., A* **1994**, *92*, 267–275.
- (25) Qazi, S. J. S.; Rennie, A. R.; Cockcroft, J. K.; Vickers, M. *J. Colloid Interface Sci.* **2009**, *338*, 105–110.
- (26) Jogun, S. M.; Zukoski, C. F. *J. Rheol.* **1999**, *43* (4), 847–871.
- (27) Idziak, S. H. J.; Welch, S. E.; Kisilak, M.; Mugford, C.; Potvin, G.; Veldhuis, L.; Sirota, E. B. *Eur. Phys. J. E* **2001**, *6*, 139–145.
- (28) COMSOL Multiphysics version 3.5a, www.comsol.com.
- (29) Clarke, S. M.; Rennie, A. R.; Convert, P. *Europhys. Lett.* **1996**, *35*, 233–238.
- (30) Spiegel, M. R., *Mathematical Handbook of Formulas and Tables*; McGraw-Hill: New York, 1968; p 146.
- (31) Pedersen, J. S. *Adv. Colloid Interf. Sci.* **1997**, *70*, 171–210.
- (32) Penfold, J.; Staples, E.; Ugazio, S.; Tucker, I.; Soubiran, L.; Hubbard, J.; Noro, M.; O’Malley, B.; Ferrante, A.; Ford, G.; Buron, H. *J. Phys. Chem. B* **2005**, *109*, 18107–18116.
- (33) Fuller, G. G.; Cathey, C. A.; Hubbard, B.; Zebrowski, B. E. *J. Rheol.* **1987**, *31*, 235–249.
- (34) Ng, S. L.; Mun, R. P.; Boger, D. V.; James, D. F. *J. Non-Newtonian Fluid Mech.* **1996**, *65*, 291–298.

Supporting information

The Alignment of Dispersions of Plate-like Colloidal Particles of **Ni(OH)₂** induced by Elongational Flow

S. Junaid S. Qazi,^{a,*} Adrian R. Rennie,^a Ian Tucker,^b Jeff Penfold^c Isabelle Grillo^d

^a Division of Materials Physics, Department of Physics and Astronomy, Uppsala University, Box 516, SE-751 20 Uppsala, Sweden

^b Unilever Research and Development, Port Sunlight Laboratory, Quarry Road East, Bebington, Wirral, U.K.

^c ISIS, Rutherford Appleton Laboratory, Chilton, Didcot, Oxon, U.K.

^d Institut Laue Langevin, F-38042 Grenoble, France

Contact author:

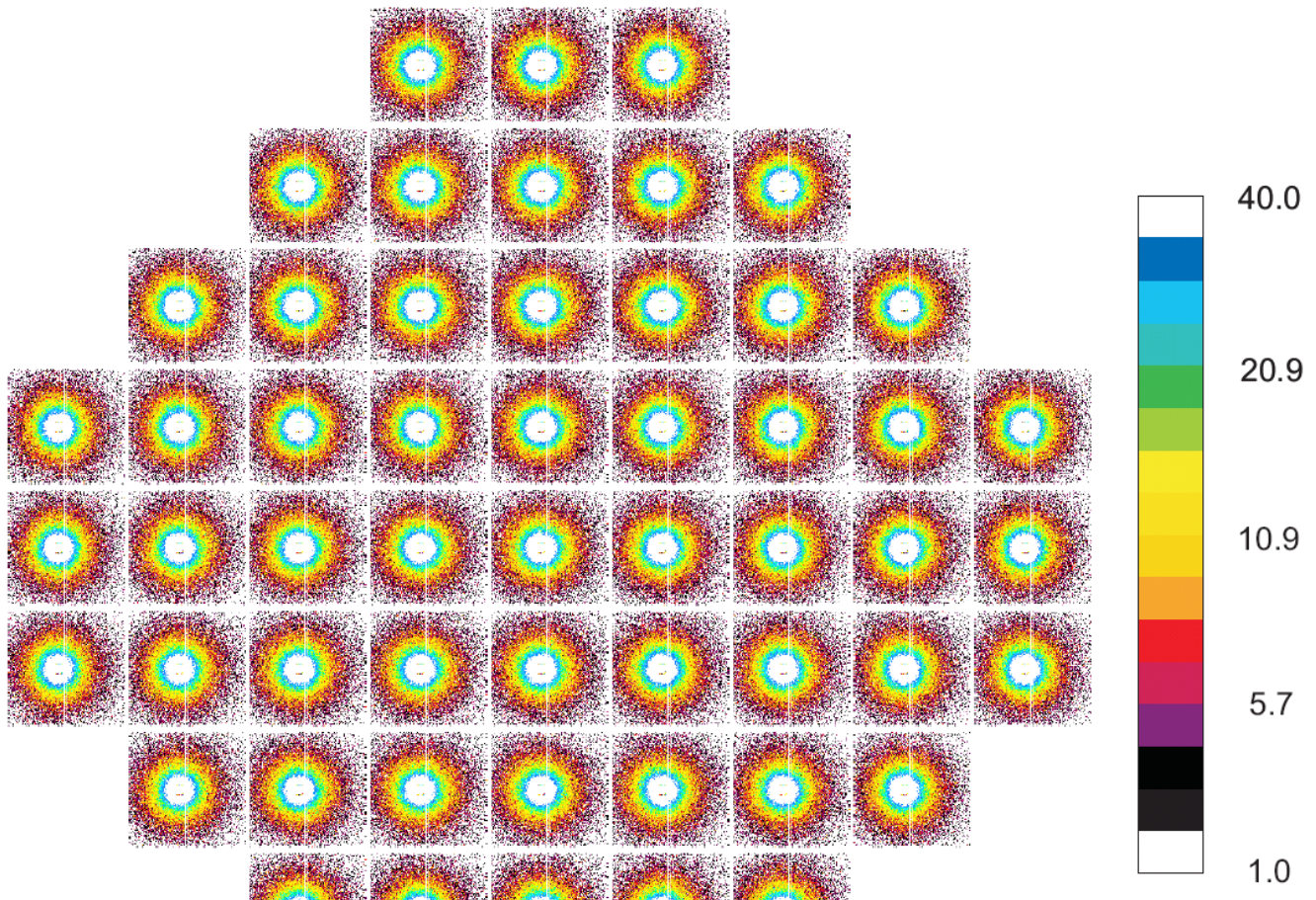
S. Junaid S. Qazi

Telephone: + 46 18 471 3522

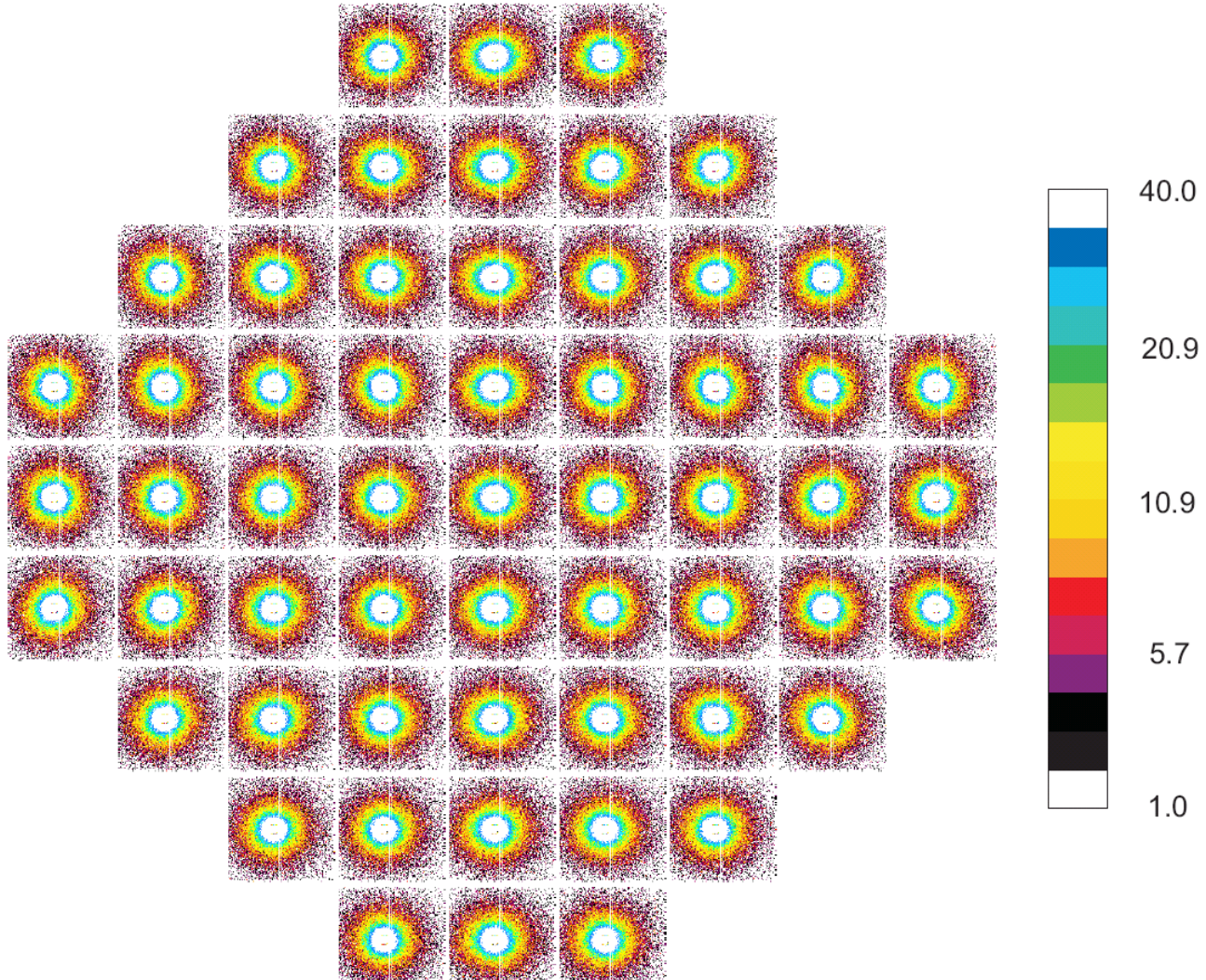
E-mail: Junaid.Qazi@fysik.uu.se

* On study leave from COMSATS Institute of Information Technology, Pakistan.

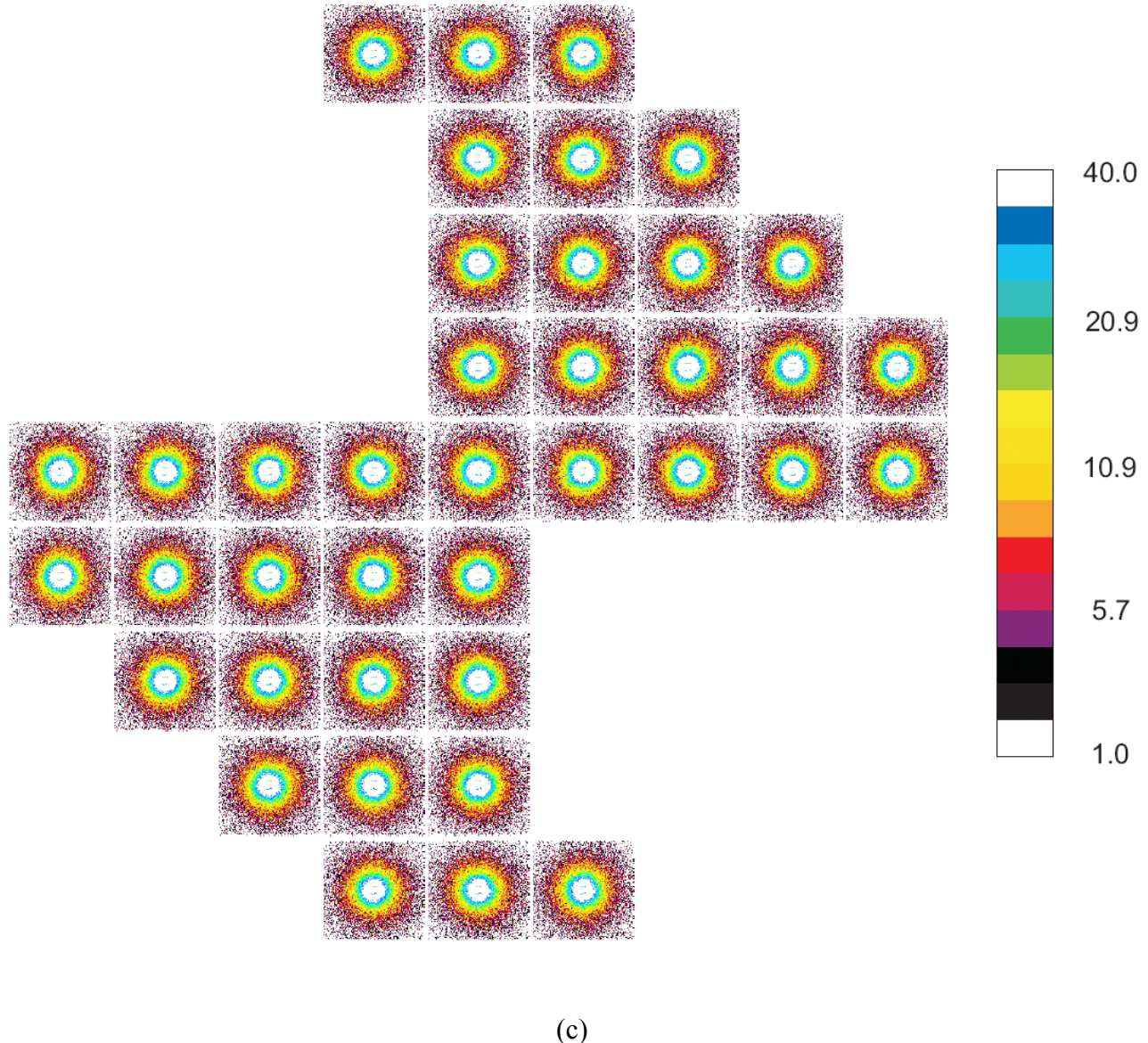
Small-angle neutron scattering (SANS) data were collected at different positions in a viewable window of the elongational flow cell as shown in Figure 1 in the main article. The center of the cell is defined as (0, 0) and the centers of neighboring scattering patterns were separated by 2 mm in the horizontal and vertical directions. Data for 23 wt % nickel hydroxide were collected at three different flow rate 4 mL s^{-1} , 12 mL s^{-1} and 15 mL s^{-1} . The scattering patterns collected as raster maps of the cell at 4 mL s^{-1} and 12 mL s^{-1} are presented in Figure S1 (a) and (b). The scattering patterns at the flow rate of 15 mL s^{-1} are shown in Figure 5 in the main article. Anisotropy in the scattering patterns increases as the flow rate increases. The order parameters S_2 for all this data are shown in Figure 6 in the main article. Figure S1(c) shows the scattering patterns measured for the sample at a slightly lower concentration (20 wt % nickel hydroxide) and the corresponding S_2 map is presented in Figure 6 (d) in the main article. The nickel hydroxide plates did not show any alignment at this concentration even at the flow rate of 28 mL s^{-1} .



(a)



(b)



(c)

Figure S1. SANS patterns for 23 wt. % $\text{Ni}(\text{OH})_2$ at the flow rates of 4 ml s^{-1} and 12 ml s^{-1} are shown in (a) and (b) respectively. Anisotropy increases in (b) as the flow rate and elongational strain rate increases. Scattering patterns for 20 wt. % nickel hydroxide concentration are shown in (c). The path length for the 20 wt. % sample was 6 mm and for 23 wt. % the path length was 3.5 mm which gives a higher elongational strain rate along the vertical axis.

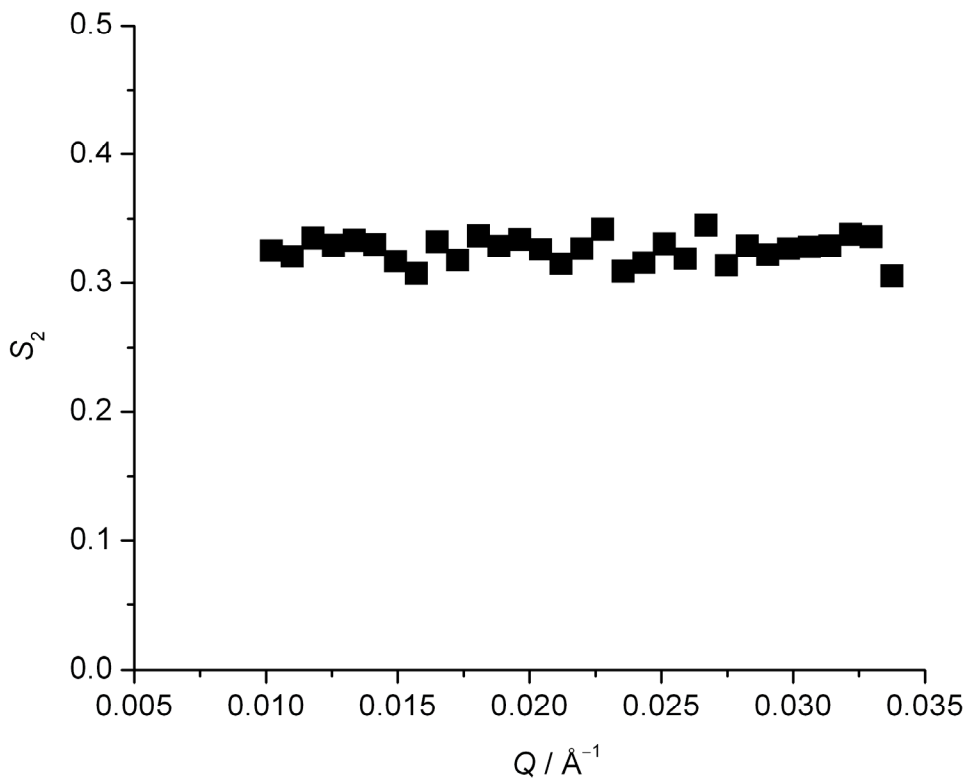


Figure S2. Values of S_2 for different Q ranges for data measured at $(0, 0)$ for the flow rate of 15 mL s^{-1} . These do not show significant differences and this allows us to use the average of S_2 over a wide Q range for interpretation of the data.

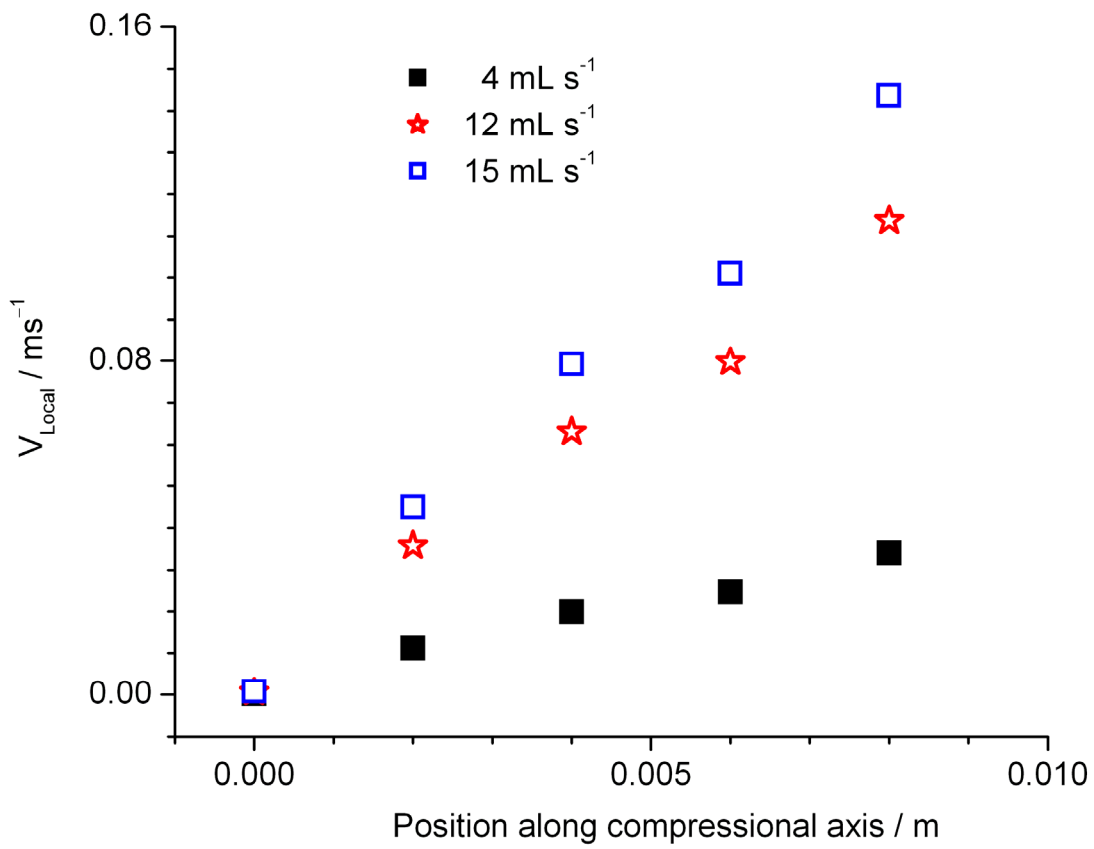


Figure S3. Local velocities, calculated from the fluid dynamics simulations, are shown at the scanned positions along the compressional axis in the elongational flow cell. Velocity decreases from maximum value to zero at a given flow rate from the inlet to the center of the cell.

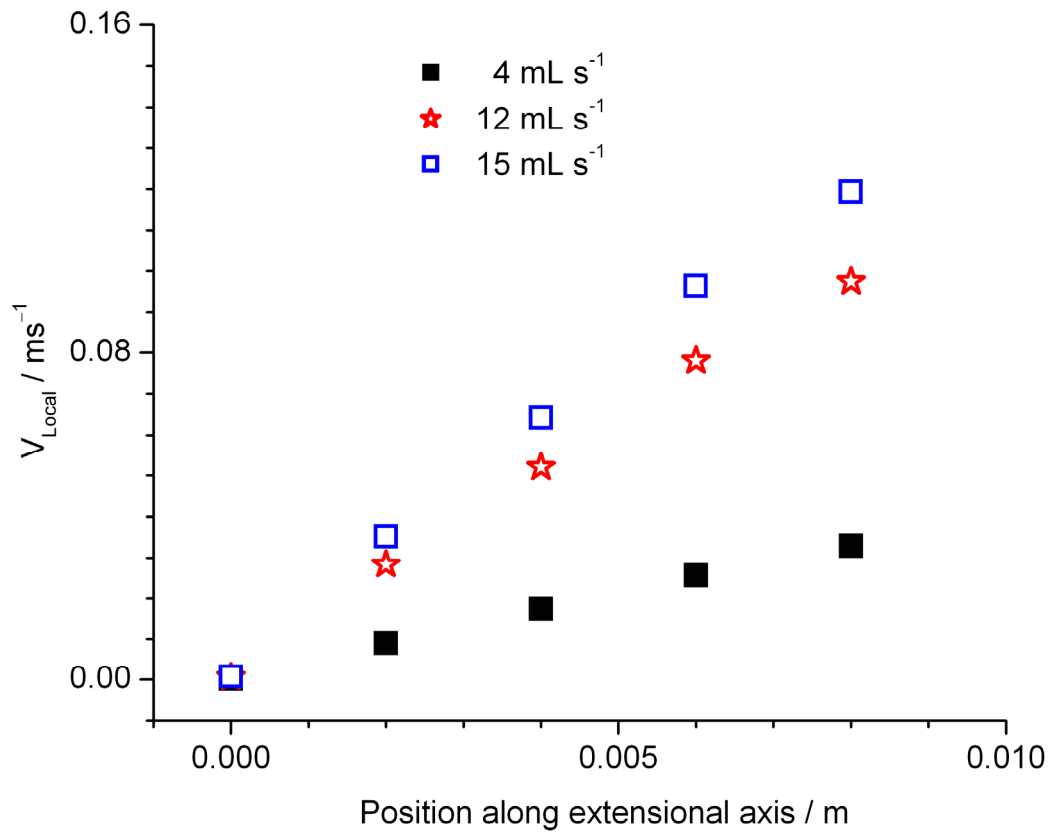


Figure S4. Local velocity increases linearly from zero to maximum value for a given flow rate from the center of the cell to the outlet. Values of the velocity are calculated from the fluid dynamics simulations along the extensional axis in the elongational flow cell.

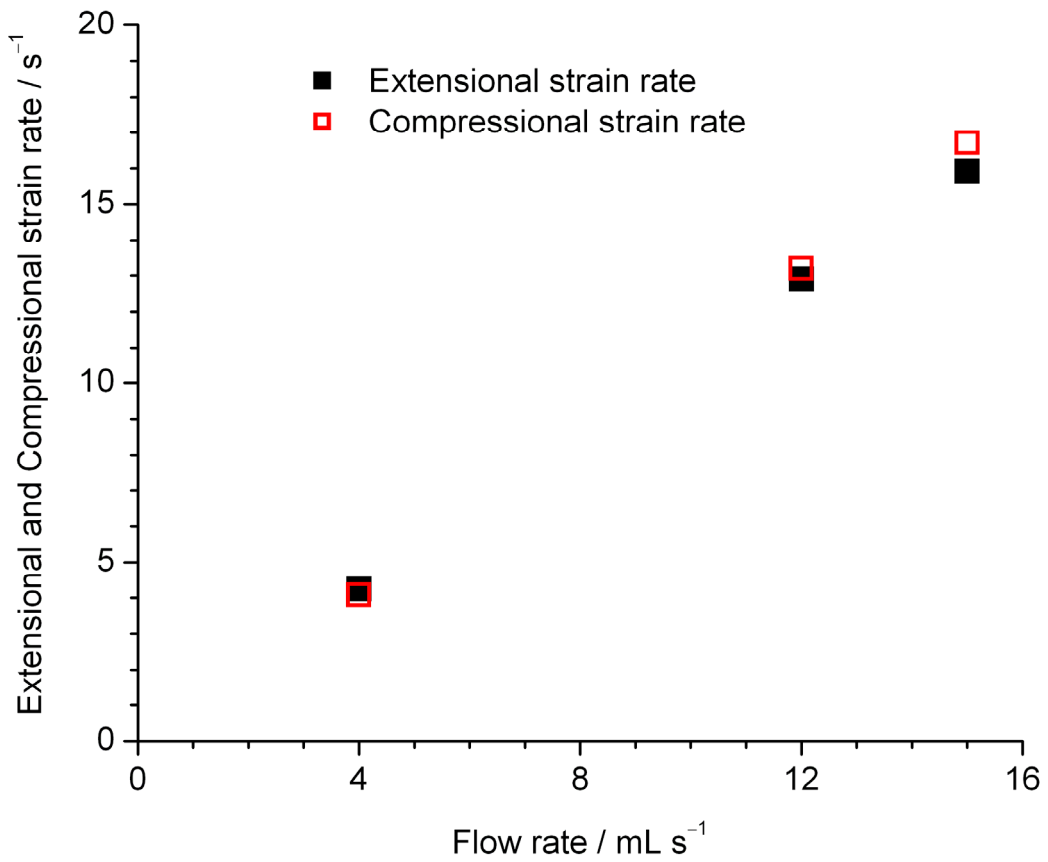


Figure S5. Strain rate calculated as the derivative of the velocity in the flow direction. Extensional and compressional strain rates increase equally as the flow rate increases in the elongational flow cell.